SUPPLEMENTAL DATA

The Basic Properties of the Electronic Structure of the Oxygen-Evolving Complex of Photosystem II are not Perturbed by Ca^{2+} Removal

Thomas Lohmiller,[‡] Nicholas Cox,[‡] Ji-Hu Su,[‡,§] Johannes Messinger,[‖] Wolfgang Lubitz[‡,1]

[‡]Max-Planck-Institut für Bioanorganische Chemie, Stiftstrasse 34-36, 45470 Mülheim an der Ruhr, Germany.

[§]Present address: Department of Modern Physics, University of Science and Technology of China, Hefei, Anhui 230026, China.

[‖]Department of Chemistry, Chemical Biological Centre (KBC), Umeå University, S-90187 Umeå, Sweden.

[1]To whom correspondence should be addressed: Prof. Dr. Wolfgang Lubitz, Max-Planck-Institut für Bioanorganische Chemie, Stiftstrasse 34-36, 45470 Mülheim an der Ruhr, Germany, Tel: +49 208 306 3614. Fax: +49 208 306 3955. E-mail: wolfgang.lubitz@mpi-mail.mpg.de.

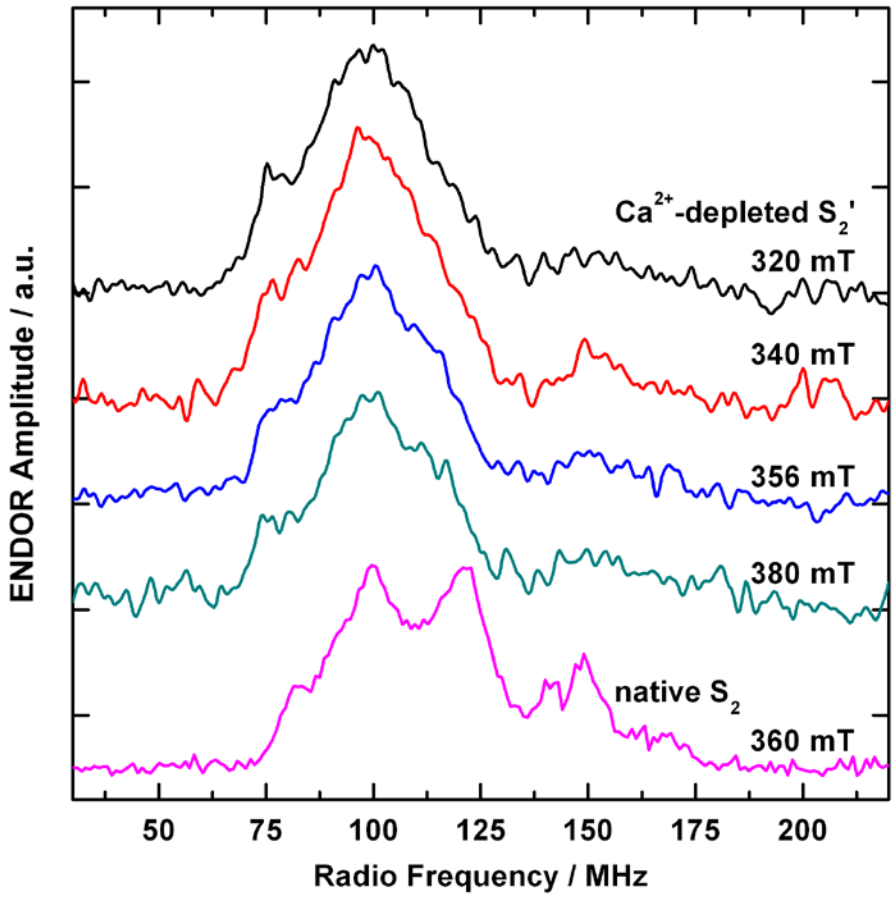

SUPPLEMENTAL FIGURE S1. X-band Davies ENDOR spectra of the Ca^{2+}-depleted OEC poised in the S_2' state in PS II isolated from spinach at various magnetic fields and, for comparison, of the native OEC in the S_2 state in the presence of 3 % MeOH at B_0 = 360 mT (bottom trace), as published in Refs. (1, 2). The S_2' state spectra were smoothed using a 9-point moving average. Experimental parameters (S_2' state): MW frequency: 9.717 GHz; shot repetition rate: 5 µs; MW pulse length π: 12 ns; τ: 200 ns; magnetic fields B_0: 320 mT, 340 mT, 356 mT, 380 mT (from the top); RF pulse length π_{RF}: 4 µs; temperature: 5 K; accumulations/time: 460/355 min, 166/149 min, 160/144 min, 339/305 min (from the top).

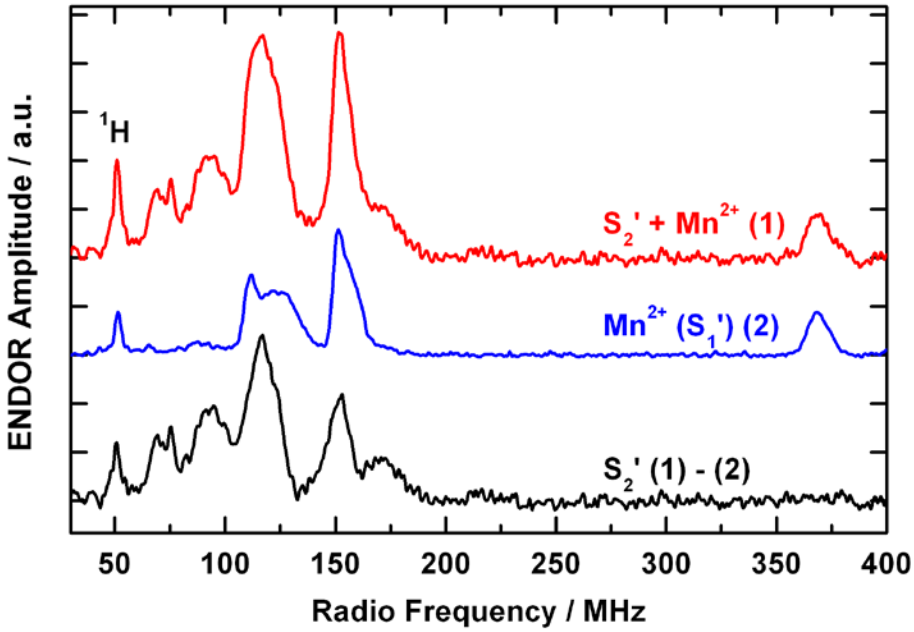

SUPPLEMENTAL FIGURE S2. Q-band Davies ENDOR spectra of Ca^{2+}-depleted PS II isolated from spinach illustrating the subtraction of the contaminating Mn^{2+} signal from the raw data obtained from the sample poised in the S_2' state, which yields the pure spectrum of the Ca^{2+}-depleted Mn_4O_5 cluster in the S_2' state. Top trace (1): Spectrum of an illuminated sample poised in the S_2' state containing both the S_2' state signal and contributions from residual Mn^{2+} ions. Middle trace (2): Spectrum of a dark-adapted sample poised in the S_1' state before illumination showing only the Mn^{2+} signal. For the subtraction, both spectra (1) and (2) were normalized with respect to the signal around 370 MHz, to which only the Mn^{2+} ion contributes. Bottom trace (1 – 2): difference of the spectra from samples in the S_2' and the S_1' states, the result of which is the spectrum of the OEC in the S_2' state. Experimental settings: MW frequency: 34.033 GHz; shot repetition rate: 5 µs; MW pulse length π: 72 ns; τ: 480 ns; magnetic field B_0: 1208 mT; RF pulse length π_{RF}: 4 µs; temperature: 5 K; accumulations/time: 202/218 min (1), 358/387 min (2).

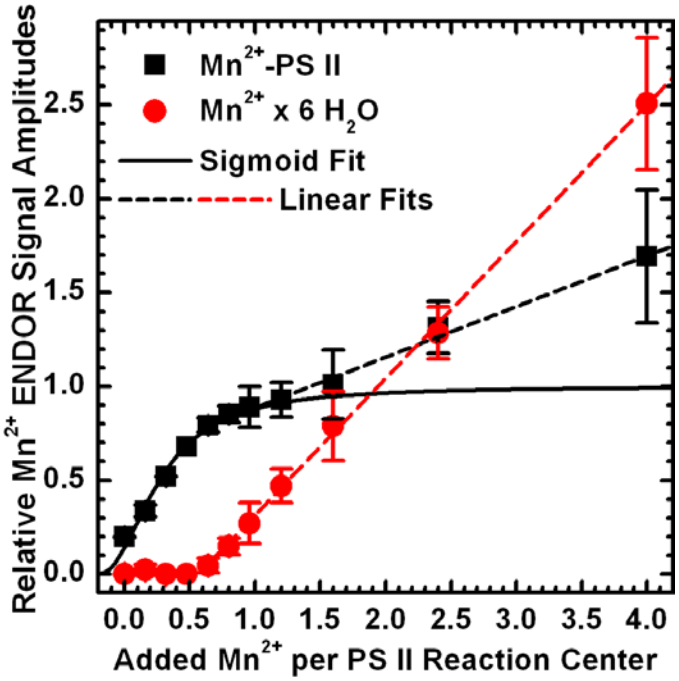

SUPPLEMENTAL FIGURE S3. Titration of dark-adapted Ca^{2+}-depleted PS II samples (S_1' state) with Mn^{2+}. The relative Q-band ^{55}Mn Davies ENDOR signal intensities of Mn^{2+} ions bound to the PS II protein complex (black squares) and hexaquo-Mn^{2+} in solution (red circles), quantified as described in the Experimental Procedures section 2.6 (main text), are plotted against the equivalents of Mn^{2+} ions added to the samples. The concentration of the defined PS II-bound Mn^{2+} species as a function of added Mn^{2+} was reproduced by means of a sigmoid curve fitted to the determined intensities up to 1.2 equivalents of Mn^{2+} in which the zero crossing of the x-axis was shifted to -0.2 equivalents with a half-binding value of 0.47 equivalents (solid line). The increase of hexaquo-Mn^{2+}, as well as additionally unspecifically bound hexaquo-Mn^{2+} ions was reproduced by linear fits to the measured intensities above 0.64 equivalents of added Mn^{2+} ions (dashed lines). The concentration of reaction centers in the samples was 25 ± 3 μM. For the experimental parameters of the ^{55}Mn Davies ENDOR measurements see Fig. 4A (main text).

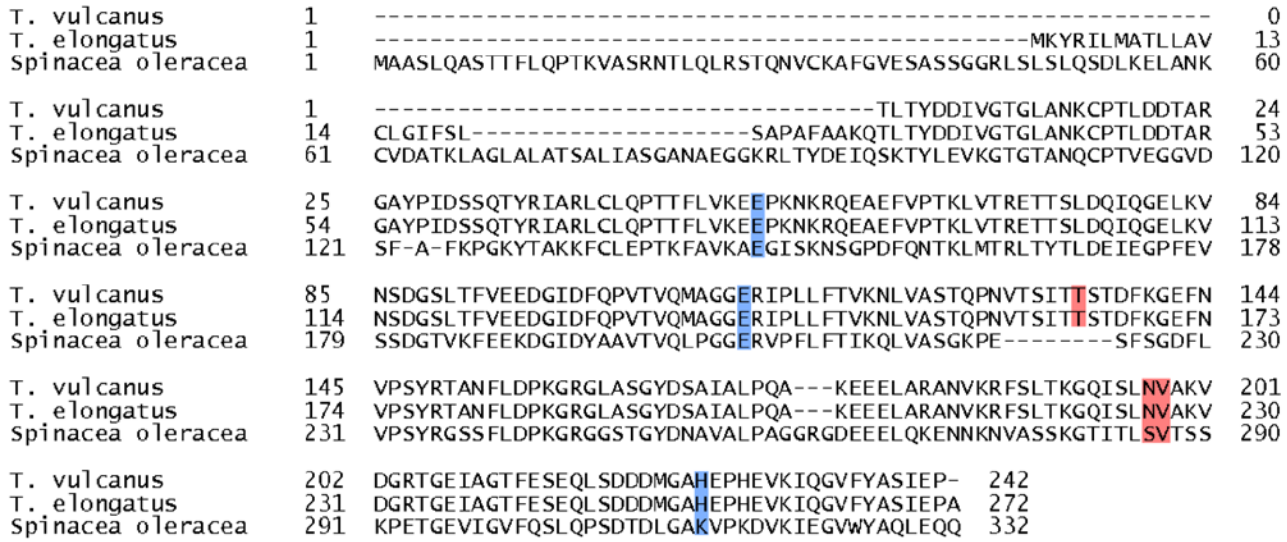

SUPPLEMENTAL FIGURE S4. Amino acid sequence alignment of the PsbO proteins from the cyanobacteria *T. vulcanus* and *T. elongatus* and the higher plant spinach (*Spinacea oleracea*). Residues ligating the Ca^{2+} ions at the sites identified in the PS II crystal structures from *T. vulcanus* and *T. elongatus* are highlighted in red and blue, respectively. The protein sequence alignment was performed using the BLAST search engine provided by UniProt (3).

SUPPLEMENTAL TABLE S1. Principal Values[a] and Isotropic[b] and Anisotropic[c] Values of the Effective G and ^{55}Mn HFI Tensors A_i (i = 1-4) for the Simulations of the X- and Q-Band EPR and ENDOR Spectra of the Ca^{2+}-depleted PS II from Spinach in the S_2' State (Fig. 2, Main Text) and for the S_2 States of Native Spinach PS II (2) and Native and Sr^{2+}-substituted PS II from *T. elongatus* (4).

			G	A_1 / MHz	A_2 / MHz	A_3 / MHz	A_4 / MHz
Spinach	-Ca^{2+} S_2'	x	1.979	342	212	173	139
		y	1.986	328	199	205	164
		$\perp$ [a]	1.983	335	206	189	152
		z ($\parallel$) [a]	1.979	263	290	227	211
		iso [b]	1.981	311	234	202	171
		aniso [c]	0.004	72	-84	-38	-59
	Ca^{2+} S_2	x	1.997	310	235	185	170
		y	1.970	310	235	185	170
		$\perp$ [a]	1.984	310	235	185	170
		z ($\parallel$)	1.965	275	275	245	240
		iso	1.977	298	248	205	193
		aniso	0.019	35	-40	-60	-70
T. elongatus	Ca^{2+} S_2	x	1.971	350	249	202	148
		y	1.948	310	227	182	162
		$\perp$ [a]	1.960	330	238	192	155
		z ($\parallel$)	1.985	275	278	240	263
		iso	1.968	312	251	208	191
		aniso	-0.025	55	-40	-48	-108
	Sr^{2+} S_2	x	1.995	343	244	200	156
		y	1.968	361	217	185	152
		$\perp$ [a]	1.982	352	231	193	154
		z ($\parallel$)	1.957	293	268	223	210
		iso	1.973	332	243	203	173
		aniso	0.025	59	-37	-30	-56

[a] The equatorial and axial G and A_i values are defined as $G_\perp = (G_x+G_y)/2$, $G_\parallel = G_z$ and $A_{i,\perp} = (A_{i,x}+A_{i,y})/2$, $A_{i,\parallel} = A_{i,z}$. [b] The isotropic G_{iso} and $A_{i,iso}$ (i = 1-4) values are the averages of the principal values: $G_{iso} = (G_x+G_y+G_z)/3$ and $A_{i,iso} = (A_{i,x}+A_{i,y}+A_{i,z})/3$. [c] The anisotropy in the G and A_i values is expressed as the differences $G_{aniso} = G_\perp - G_\parallel$ and $A_{i,aniso} = A_\perp - A_\parallel$ between the perpendicular and parallel components of the tensors.

Correlation between the ground-to-first excited state energy difference Δ and the temperature dependence of the intensity I_1 of the ground spin state EPR signal. The relative intensity I_1 of the ground spin state signal I_1 depends on the inverse temperature weighted by the Boltzmann factor:

$$I_1 = \frac{C}{T}\frac{(2S_1+1)\exp(-E_1/kT)}{\sum_i (2S_i+1)\exp(-E_i/kT)} \qquad \text{(S1)}$$

where C is a proportionality constant, S_i represents the total spin of the coupled states of the spin manifold (S = 1/2, 3/2, …..) and E_i are the respective energies. Here, a two spin model is used to describe the energy ladder in terms of a single effective coupling constant, J_{eff} between two fragments of the Mn tetramer: monomeric Mn_{A4} (Mn^{IV}, S_{A4} = 3/2), and the coupled trimer $Mn_{B3}Mn_{C2}Mn_{D1}$ ($Mn^{III}(Mn^{IV})_2$, spin ground state $S_{B3\text{-}C2\text{-}D1}$ = 1 or 2), see (5). The corresponding simplified Hamiltonian $H = -J_{\text{eff}}S_{A4}S_{B3\text{-}C2\text{-}D1}$ gives spin state energies $E_i = (S_{A4}(S_{A4}+1) + S_{B3\text{-}C2\text{-}D1}(S_{B3\text{-}C2\text{-}D1}+1) - S_i(S_i+1))J_{\text{eff}}$, where the total spin $S_i = (S_{A4} - S_{B3\text{-}C2\text{-}D1})\ldots(S_{A4} + S_{B3\text{-}C2\text{-}D1}) = 1/2\ldots5/2$. Equation S1 can thus be used to estimate J_{eff} and $\Delta = E_2 - E_1 = -3J_{\text{eff}}$.

Effect of the Zero-Field Splitting Interaction on the Spin States and EPR and ^{55}Mn ENDOR Signals of Mn^{2+} Complexes (see also (6)*).* The EPR and ^{55}Mn ENDOR signals originating from the Mn^{2+} ions bound to Ca^{2+}-depleted PS II differ substantially from those typically associated with mononuclear Mn^{2+} species in that they appear significantly broadened by the large and strongly rhombic ZFS (Figs. 3 and 4A in the main text). The characteristic EPR spectrum of high-spin $S = 5/2$ Mn^{2+} complexes is the six-line signal with a HFI splitting of ~9 mT. For the ^{55}Mn nucleus of nuclear spin $I = 5/2$, each of these lines can be assigned to one nuclear spin sublevel m_I ranging from -5/2 to +5/2. The corresponding ^{55}Mn ENDOR signal contains 3 orientation-selective doublets centered roughly around ~125, ~375 and ~625 MHz, which originate from nuclear transitions within the m_S = |1/2|, |3/2| and |5/2| electronic submanifolds, respectively.

In the absence of a ZFS interaction, a $^{55}Mn^{2+}$ EPR spectrum consist of six separate lines associated with one m_I sublevel, to each of which the five $\Delta m_S = \pm 1$ transitions contribute. The ZFS leads to an anisotropic broadening of these transitions, especially those involving manifolds of electronic spin substates $|m_S| > 1/2$. Additionally, the symmetry of the ZFS tensor has a considerable effect on the orientation-dependence and thus on the line width. A large rhombicity of this interaction enhances the broadening of the powder patterns. As the ZFS becomes more relevant, the transitions associated with a certain m_I are increasingly overlapping, such that it comes to a spreading of the entire spectrum. To some extent, the broadening may additionally be attributed to small site-to-site inhomogeneities of the Mn^{2+} environment, which have an immediate effect on the spin Hamiltonian parameters and are especially found in large and dynamic biological systems like proteins. These effects add up to result in the very broad, featureless spectrum, in which the six-line hyperfine structure from $|m_S| = 1/2$ transitions is not resolved.

The pulse ENDOR spectra are directly affected by this spread. In the absence of a ZFS, the transitions involving a particular m_I can be probed individually by selective irradiation at frequency and field of one of the six EPR lines. Therefore, six different ^{55}Mn ENDOR spectra can be measured, each of them only comprising the transitions corresponding to the selected nuclear spin m_I, associated with all six m_S

sublevels. In case of a ZFS-induced anisotropic spread of the m_S substate energies, the relative intensities of the ENDOR lines from the six m_S substates for a particular m_I become orientation-selective. In Fig. 4 (main text), the high-frequency m_S = -3/2 signal intensities relative to those of the low-frequency m_S = -1/2 and m_S = +1/2 signals are clearly smaller at the more central field positions in the EPR spectrum, the spectra at 1208 mT and 1224 mT, compared to the outer ones. At 1195 mT and 1260 mT, there is a stronger relative contribution from the m_S = -3/2 transitions due to their larger spread by the ZFS. Furthermore, the overlapping transition energies of the different m_I manifolds result in spectra comprising the ENDOR transitions of more than one m_I value, which leads to a broadening and concomitant lowering of the structural resolution of ENDOR lines. This reduced m_I selectivity can be clearly seen in these very broad ^{55}Mn ENDOR spectra where no spectral structure of single m_I transitions is resolved. Due to the large energetic spread in the case of the high-spin m_S = -3/2 sublevels, even all five corresponding m_I transitions are excited at the same time.

The Electronic Structure of an Effective S = 1/2 Spin State System: Relation of Effective Tensor Properties and Non-Explicitly Treated Interaction Terms. For evaluation of the intrinsic ZFS values d_i of the Mn ions resulting from the obtained electronic exchange coupling scheme (Fig. 7 in the main text) and whether these are within the reasonable ranges for the individual Mn oxidation states, a short overview is given on how they are calculated based on the inferred coupling topology and experimental effective spin Hamiltonian parameters:

Same as for the Ca^{2+}- and Sr^{2+}-containing S_2 states, the coupled Mn electronic spin system of the Ca^{2+}-depleted S_2' state can be described by an effective spin Hamiltonian (see the Experimental Procedures section 2.5), which does not include any pair-wise interaction terms such as the Heisenberg-Dirac-Van Vleck operator for the electronic exchange interaction and the ZFS term. Thus, the fitted *G* and HFI tensors A_i (Table 2 in the main text, supplemental Table S1) also represent effective tensors. However instead, the corresponding intrinsic (on-site) HFI tensors a_i need to be considered for comparison to values reported for other Mn systems, assignment of oxidation states and conclusions about coordination geometries of individual Mn ions. Effective and intrinsic properties of each Mn_i ion are related by a spin projection coefficient ρ_i, a measure of the contribution of Mn_i to a particular spin state. The tensor components of this scaling factor are the ratio of the corresponding effective and intrinsic values, i.e. $\rho_i = A_i / a_i$ for the HFI. The effective *G* tensor, as a property of the effective electron spin *S* of the Mn cluster, is a weighted linear sum of the intrinsic *g* tensors of the individual Mn ions $G = \sum \rho_i g_i$. As they map the subspace of the effective spin state to the entire configuration space, the ρ_i tensors for oligomeric spin systems can be computed based on the spin coupling scheme in the form of pair-wise electronic exchange interaction terms between all of the four Mn ions. Therein, the ZFS interaction, not considered explicitly as a term of the spin Hamiltonian, can be taken into account such that it affects the ρ_i tesors in an orientation-dependent manner. Through the exchange coupling between the electronic spins, the intrinsic ZFS value d_i of one Mn ion influences the ρ_j tensors of the others, too, which thus can be envisaged as a transfer of anisotropy to the other Mn ions in the cluster (for more detailed information see Refs. (4, 7, 8)).

REFERENCES

1. Kulik, L., Epel, B., Messinger, J., and Lubitz, W. (2005) *Photosynth. Res.* **84**, 347–353
2. Kulik, L. V., Epel, B., Lubitz, W., and Messinger, J. (2007) *J. Am. Chem. Soc.* **129**, 13421–13435
3. The UniProt Consortium (2011) *Nucleic Acids Res.* **40**, D71–D75
4. Cox, N., Rapatskiy, L., Su, J.-H., Pantazis, D. A., Sugiura, M., Kulik, L., Dorlet, P., Rutherford, A. W., Neese, F., Boussac, A., Lubitz, W., and Messinger, J. (2011) *J. Am. Chem. Soc.* **133**, 3635–3648
5. Su, J.-H., Cox, N., Ames, W., Pantazis, D. A., Rapatskiy, L., Lohmiller, T., Kulik, L. V., Dorlet, P., Rutherford, A. W., Neese, F., Boussac, A., Lubitz, W., and Messinger, J. (2011) *Biochim. Biophys. Acta, Bioenerg.* **1807**, 829–840
6. Sturgeon, B. E., Ball, J. A., Randall, D. W., and Britt, R. D. (1994) *J. Phys. Chem.* **98**, 12871–12883
7. Peloquin, J. M., Campbell, K. A., Randall, D. W., Evanchik, M. A., Pecoraro, V. L., Armstrong, W. H., and Britt, R. D. (2000) *J. Am. Chem. Soc.* **122**, 10926–10942
8. Schäfer, K.-O., Bittl, R., Zweygart, W., Lendzian, F., Haselhorst, G., Weyhermüller, T., Wieghardt, K., and Lubitz, W. (1998) *J. Am. Chem. Soc.* **120**, 13104–13120